Journal of Building Engineering 114 (2025) 114244

Contents lists available at ScienceDirect

Journal of Building Engineering

journal homepage: www.elsevier.com/locate/jobe

Improved method for UV lamps irradiance characterization and life-cycle assessment for in-duct microbial inactivation

Jay Patel, Sunday S. Nunayon, Lexuan Zhong *

Department of Mechanical Engineering, University of Alberta, Edmonton, Alberta, Canada

ARTICLE INFO

Keywords:
HVAC
Indoor air quality (IAQ)
In-duct air disinfection
Irradiance characterization
Novel correction factor
Life cycle assessment (LCA)
Ultraviolet germicidal irradiation (UVGI)

ABSTRACT

Accurate characterization of ultraviolet (UV) irradiance is essential for the effective design and evaluation of in-duct air disinfection systems. This study aims to develop a novel angular correction factor to address sensor detection-angle limitations. Experimental irradiance measurements were conducted for 222 nm excimer lamp, 254 nm mercury lamp, 265 nm UVC LED and 365 nm UVA LEDs, and their environmental sensitivity was assessed under varying air temperature, velocity, and relative humidity. The comparative life-cycle assessment evaluated energy, costs, and environmental impacts for achieving a 3-log microbial reduction. Findings show that the correction factor reduced overestimation by up to 30 % near lamp surfaces, with a maximum error (18 %) observed farther from the 254 nm lamp. Model-based scalability from single LED modules to full arrays yielded an average relative error of ±13 %, supporting flexible LED arrangements. The 254 nm lamp output increased by 18 % as air temperature rose (25–35 °C) and decreased nearly to 80 % as velocity increased (0.5–2 m/s). In contrast, the 222 nm lamp and both LED systems showed minimal sensitivity, indicating greater operational stability under dynamic conditions. While LEDs and 222 nm offer their own advantages, they require higher energy and cost to achieve equivalent disinfection. Therefore, under continuous in-duct application, the 254 nm lamp is the most sustainable and cost-effective option among those tested. This study provides a validated, building-scale framework that improves measurement accuracy and supports energy-aware implementation, offering actionable guidance for optimized, sustainable deployment of UVGI in building ventilation systems.

1. Introduction

Indoor air quality (IAQ) plays a critical role in determining occupant health and well-being [1]. In modern buildings, heating, ventilation, and air conditioning (HVAC) systems are essential for delivering clean, conditioned air. However, HVAC components such as filters, ducts, coils, humidifiers, and cooling towers can become sources of contamination, particularly under conditions of high humidity and inadequate maintenance [2–4]. A major concern is the potential of HVAC systems to transport bioaerosols emitted by occupants, thereby facilitating airborne transmission of infectious agents.

Filtration units integrated into HVAC systems are commonly employed to capture airborne contaminants originating from both indoor and outdoor sources. Their performance is typically rated using the Minimum Efficiency Reporting Value (MERV), which ranges from 1 to 20 and indicates a filter's ability to capture particles (≥10 μm to ≤0.3 μm) [1]. However, medium-efficiency filters (MERV

---

* Corresponding author.
E-mail address: lexuan.zhong@ualberta.ca (L. Zhong).

https://doi.org/10.1016/j.jobe.2025.114244
Received 17 June 2025; Received in revised form 31 August 2025; Accepted 30 September 2025

5–9) [2] have limited effectiveness against smaller airborne pathogens such as viruses and bacteria [3]. Furthermore, increasing ventilation rates or upgrading to HEPA filtration is often economically unfeasible for many general building applications [4]. Given the substantial health risks posed by airborne pathogens [5], there is a growing demand for cost-effective and sustainable in-duct disinfection technologies to complement conventional filtration and ventilation strategies [6].

Ultraviolet germicidal irradiation (UVGI) offers a promising proactive approach to microbial air disinfection [7,8]. UVC light (200–280 nm), particularly around 260–265 nm, exhibits peak germicidal effectiveness due to the strong absorption of this wavelength by nucleic acids, leading to disruption of DNA/RNA and protein structures. Traditional low-pressure mercury (LP Hg) lamps emitting at 254 nm closely align with this peak and are widely used [9–11]. More recently, far-UVC (e.g., 222 nm) filtered excimer lamps have gained attention due to their strong antimicrobial efficacy combined with limited tissue penetration, which offers enhanced safety for occupied spaces [12]. In contrast, wavelengths above 280 nm, typically produced by UV LEDs, have lower germicidal effectiveness due to reduced nucleic acid absorption.

In addition to wavelength, UVGI performance depends on UV fluence—the product of irradiance (mW/cm^2) and exposure time (s). In-duct UVGI systems have demonstrated effectiveness in reducing microbial loads in air-handling systems, but accurately characterizing the irradiance field under realistic HVAC conditions remains an engineering challenge. Turbulent airflow, prevalent in operational ducts, reduces bioaerosol residence time and complicates uniform exposure. Many prior studies on UVGI efficacy have been conducted under laminar or simplified flow regimes ($Re < 700$), limiting their relevance to real-world scenarios. Furthermore, the interaction of UV lamp geometry, spatial arrangement, duct materials, and turbulent flow patterns significantly affects irradiance distribution and system effectiveness.

Reliable irradiance estimation is critical for UVGI system optimization. Computational methods, such as view factor models, trigonometric functions, or simulations, offer precision but are resource-intensive and unsuitable for routine design applications [11]. Experimental approaches using radiometers, photometers, or spectrometers are more accessible but often measure planar irradiance and are not suited for capturing omnidirectional fields, particularly in reflective enclosures. To approximate volumetric irradiance, some studies measure it from all six planner directions within the duct and sum the values, often neglecting the limits of the sensors' angular sensitivity, leading to potential overestimation [12–18]. Experimental characterization becomes even more complex with UV-LED arrays due to their spatial variability and directional emission, and no standardized framework currently exists for this purpose.

Environmental conditions such as airflow velocity, temperature, and relative humidity (RH) further complicate UVGI system performance. These parameters critically affect lamp output and disinfection efficacy [11,15]. For instance, airflow velocity influences bioaerosol residence time, while temperature affects LP Hg lamps, with optimal performance typically occurring near 40 °C [13]. UV LEDs are especially sensitive to temperature, with optical output declining by up to 25 % as junction temperatures increase from 20 °C to 120 °C [19–21]. Although one manufacturer reports stable performance across moderate temperature ranges (e.g., 20–60 °C) [22], such claims are typically based on water disinfection and may not extend to air-based applications. Likewise, RH has been shown to variably enhance, diminish, or have no measurable effect on UVC lamp output [11,13,15,23], and these inconsistencies complicate optimization efforts. In real HVAC systems, where RH can exceed 60 % near cooling coils during summer, these environmental influences are especially pronounced.

A further challenge is that UV lamp manufacturers usually report performance under idealized laboratory conditions, limiting the applicability of these data in diverse operational settings. This contributes to the persistent discrepancy between laboratory efficacy and field performance. Additionally, most existing studies have focused on cylindrical low-pressure mercury lamps, with limited frameworks available for characterizing the more complex irradiance fields of emerging technologies such as UV-LED arrays and far-UVC lamps. As these technologies gain popularity, a significant knowledge gap remains regarding their behavior under realistic air-handling conditions. Despite rising interest in UVGI, comprehensive life cycle assessments (LCAs) comparing various UV lamp technologies under standardized disinfection scenarios are still scarce. This lack of robust comparative data impedes informed design decisions and broader adoption.

Accordingly, this study develops and validates a building-scale framework for in-duct UV dose characterization and UV lamp technology selection that: (i). Introduces a novel angular correction factor for irradiance mapping, which accounts for sensor detection-angle limits and duct-wall reflections; (ii). Experimentally evaluates the effects of environmental parameters (air

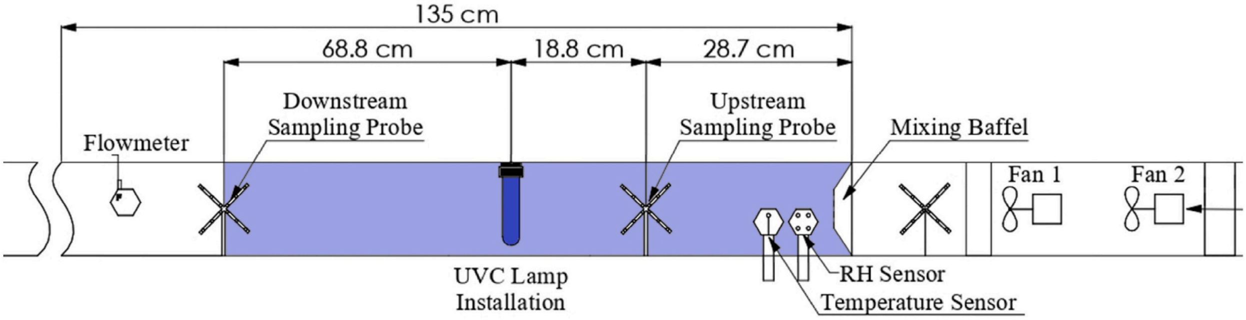

Fig. 1. Schematic of pilot scale HVAC duct setup used for UV lamp installation and irradiance characterization duct Setup.

temperature, velocity, and relative humidity, RH) on lamp performance; and (iii). Compares 254 nm low-pressure mercury, 222 nm far-UVC excimer, and UV LEDs (265 nm & 365 nm) for irradiance efficiency, energy use, cost, and operational sustainability via life-cycle assessment (LCA). By integrating performance testing with operational LCA, the study provides practical guidance for the design, optimization, and evaluation of UVGI systems in HVAC ducts, thereby advancing indoor environmental quality (IEQ) and energy-aware, sustainable building practice.

2. Methodology

2.1. Pilot scale duct set-up

A custom-built pilot-scale stainless steel duct system (12.7 cm × 12.7 cm) was developed for UV lamp installation and irradiance characterization. The setup includes essential components such as fans, filters, UV lamps, a mixing baffle, and dedicated ports for aerosol injection and sampling (Fig. 1). Environmental conditions, such as air velocity, temperature, and RH, are regulated using a feedback control system (Opto 22). Pre-qualification tests, including leakage, airflow uniformity, and aerosol distribution for the experimental rig, have been reported elsewhere [24] to ensure compliance with ASHRAE Standard 185.1–2020.

2.2. Lamp installation

Four UV lamp types were evaluated in this study: a LP Hg lamp (254 nm), a far-UVC filtered excimer lamp (222 nm), UVC LEDs (265 nm), and UVA LEDs (365 nm). These lamps were categorized into two groups based on their geometry: Cylindrical lamps (254 nm; 222 nm), and UV LEDs (265 nm; 365 nm). The normalized spectra emission of the various lamps can be referred to in Fig. S1.

2.2.1. Cylindrical lamps (254 nm & 222 nm)

The 254 nm LP Hg lamp (OSRAM GCF5DS, 5 W X 1) and 222 nm far-UVC filtered excimer lamps (Cure-UV 510100–20, 20 W X 2) were installed in the same x-y plane along the duct's total exposure length of 108 cm, divided into upstream (47.4 cm) and downstream (60.6 cm) sections. The 254 nm LP Hg lamp (12 mm diameter) was placed centrally, while the 222 nm lamps (35 mm diameter) were installed symmetrically (Fig. S2).

2.2.2. UV LEDs (265 nm & 365 nm)

Six 265 nm UVC LED modules (BOLB 2p2s SMD, 10 W each) were mounted on the left- and right-side walls of the duct using an opposite-facing configuration (Fig. S3a and S3b), with active heat sink and thermal paste for cooling.

The 365 nm UVA LEDs strip (Waveform PN 7021, 17 W/m) was divided into seven 14.2 cm modules and arranged in a zigzag pattern: four on the left wall and three on the right (Fig. S3c and S3d), forming a continuous distribution along the duct length. Overall, it forms a continuous zigzag pattern of UVA LED throughout the duct.

2.3. Irradiance measurements

2.3.1. Cylindrical lamps

Irradiance (mW/cm^2) was measured using a calibrated ILT 960 spectrometer (International Light Technologies, USA) with measurement uncertainties of ±10 % for 254 nm and ±15 % for 222 nm. After a 100-h burn-in, measurements were conducted at room temperature (20 °C ± 0.5 °C) on nine vertical planes (five downstream, four upstream), aligned perpendicularly to airflow (Fig. S4a). Each plane was divided into 3 × 3 grids, and a 9-point average irradiance was calculated (Fig. S4b). Though all six sides ideally contribute to total exposure, preliminary tests showed negligible readings from the rear (lamp-opposing) side; therefore, only five sides (front, top, bottom, left, and right) were measured three times to ensure repeatability. Details of measured irradiance are available in Table S1 and S2.

2.3.2. UV LEDs

Unlike cylindrical lamps, LEDs were characterized in the duct's width direction, perpendicular to each LED module. The measurement uncertainty of the ILT960 spectrometer was ±10 % at 265 nm and ±5 % at 365 nm. Given the complexity of full-array measurement, this study proposes a simplified predictive framework based on single-module characterization. The key assumption is that all modules exhibit symmetric irradiance profiles, and their exposure region in the duct is also similar.

For 265 nm LEDs, irradiance was measured on 10 downstream planes (totaling 20.5 cm) using 4 × 3 grids (Fig. S5a and S5b). Similarly, for 365 nm LEDs, 11 downstream planes were measured over a 29.5 cm exposure region (Fig. S6a and S6b). Measurements were taken from all six sides and repeated three times for consistency. Table S3 and S4 show the final irradiance values at each measurement location. Using regression analysis, irradiance trends for single modules were established. These trends enable the extrapolation of irradiance at any point in the duct by summing the individual contributions from symmetrically placed modules, based on their relative distance.

After baseline measurements at room temperature (20 °C ± 1 °C) for all the UV lamps, tests were conducted under varying air velocity: 0.5–2.0 m/s (T = 25 °C, RH = 40 %), air temperature: 25–35 °C (v = 0.5 m/s, RH = 40 %), and RH: 25–60 % (v = 0.5 m/s, T = 25 °C). Irradiance was measured three times in each condition to account for power fluctuations and ensure reproducibility.

2.4. Novel correction factor for irradiance calculation

Most radiometric sensors do not capture light from all 360° directions. The ILT960 spectrometer used in this study features a cosine-corrected diffuser with a practical detection angle of ±60°. Beyond this range, measurement accuracy degrades due to more than 10 % deviation from the ideal cosine response, and the measured values become negligible. To prevent irradiance overestimation caused by angular overlaps when measuring from adjacent sides (Fig. 2), a correction factor was developed:

$$C_i = \left(1 - \frac{\sum_{j=1}^{2} \varnothing_j}{\left(\sum_{j=1}^{2} j\right) * 2 * \theta}\right) \tag{1}$$

where, C_i is the correction factor for irradiance from side, i; $\varnothing_j$ represents total overlap angle in direction j, θ is the total detection angle limit (120°) and j is the direction of planner measurement, x and y.

The irradiance at a point can be calculated from the following equation.

$$I = C_\mathrm{f} I_\mathrm{f} + C_\mathrm{l} I_\mathrm{l} + C_\mathrm{r} I_\mathrm{r} + C_\mathrm{t} I_\mathrm{t} + C_\mathrm{b} I_\mathrm{b} + C_\mathrm{bc} I_\mathrm{bc} \tag{2}$$

where, I is the total average irradiance at a specific point; I_i connotes measured irradiance from side i; (f = front side; l = left side; r = right side; t = top side; b = bottom side, bc = back side). For cylindrical lamps, $C_\mathrm{f} = 0.75$; $C_\mathrm{bc} = 0$; $C_\mathrm{l} = C_\mathrm{r} = C_\mathrm{t} = C_\mathrm{b} = 0.8125$. For UV LEDs, $C_\mathrm{f} = C_\mathrm{l} = C_\mathrm{r} = C_\mathrm{t} = C_\mathrm{b} = C_\mathrm{bc} = 0.75$

To evaluate the impact of the proposed correction factor on irradiance accuracy, a statistical comparison was performed using irradiance values for the 254 nm lamp, obtained through three approaches: (1) from all five sides with correction, (2) from all five sides without correction, and (3) from a single side facing the lamp (front side only).

2.5. Exposure time and UV dose characterization

While exposure time is typically estimated by assuming uniform flow and dividing the UV-irradiated length by average airflow velocity, this assumption does not hold in the present study. The presence of cylindrical UV lamps and a mixing baffle at the inlet introduces significant flow non-uniformities. To address this, a computational fluid dynamics (CFD) approach, as described by Luo and Zhong (2022) [25], was adopted to accurately determine the exposure time of bioaerosols within the duct. The duct and lamp geometries were modelled using locally refined, unstructured meshes near the inlet and around lamp surfaces. A grid independence study was conducted for the 254 nm lamp setup, resulting in an optimal mesh resolution of approximately 694,000 cells. Airflow simulations were carried out under steady-state, isothermal conditions using a realizable k-ε turbulence model with standard wall functions. Details of the CFD approach adopted can be referred to in Text S1, Table S5, and Fig. S7 of the Supplementary Material.

The obtained trajectory data were processed using MATLAB R2022b, and average particle velocities were computed between consecutive cross-sectional planes spaced 1 mm apart. Particles with negative axial velocities (i.e., backflow) were excluded. The local exposure time between each pair of planes was calculated using the particle velocities, and this exposure time was multiplied by the experimentally measured average irradiance between the same pair of planes to determine the local UV dose. The cumulative UV dose was obtained by summing these values across the entire UV-irradiated region, thus quantifying the total dose received by airborne

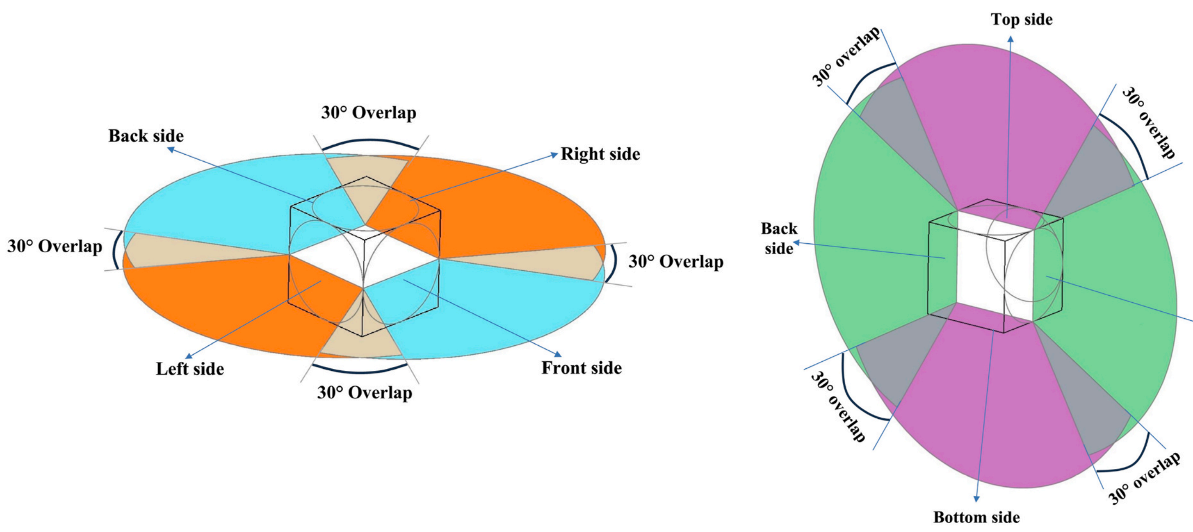

Fig. 2. Overlapped measured irradiance between the adjacent sides due to the sensor's detection angle limit.

particles [27]. The spatial distribution of the average UV dose (mJ/cm^2) along the duct length was evaluated at a mean air velocity of 1.35 m/s, with local exposure times superimposed onto the experimentally derived irradiance field.

Finally, uncertainty in UV dose estimation was quantified by propagating errors from irradiance measurement and airflow velocity using the root-sum-square method (details in Text S2). Spectrometer accuracy (±10 % at 254 nm, ±15 % at 222 nm, ±10 % at 265 nm, and ±5 % at 365 nm) and average experimental measurement and modelling errors were combined to estimate average irradiance uncertainty. These were then propagated with velocity variation (±10 %), yielding overall UV dose uncertainties for each lamp type.

2.6. LCA

To evaluate the sustainability and cost-effectiveness of various UVGI technologies for HVAC systems, an LCA was performed. The analysis focuses on the representative UV lamp types considered in this study, taking into account their unique operational characteristics and disinfection mechanisms. To establish a scientifically representative basis for UVGI performance comparison, three microbial surrogates: *Escherichia coli (E. coli)*, MS2 and Phi6 bacteriophages, were selected due to their well-characterized response to UVC exposure. This combination of surrogates ensures that the disinfection efficacy assessment is comprehensive and conservatively applicable across a broad spectrum of airborne pathogens.

The LCA includes two major cost components: initial cost and operational cost. The initial cost encompasses the lamp unit and any required accessories or drivers. For simplification and standardization, it is assumed that no additional fixture costs were incurred. The cost of accessories was considered only for UV LED systems. The initial cost was calculated using Equation (3) for all the lamps used in this study (see Tables S6, S7, S8, and S9).

$$\text{Initial Cost} = \text{Lamp Price} + \text{Accessory Cost} \tag{3}$$

The operational cost reflects the electricity consumed throughout the effective lifespan of each lamp, defined by its L70 lifetime, the point at which the lamp's output drops to 70 % of its original intensity. The operational cost was estimated as:

$$\text{Annual Operational Cost} = \text{E} \times \text{P}_\text{e} \tag{4}$$

where E is the annual electricity consumption (kWh), and P_e is the unit cost of electricity, taken as CAD 0.1205/kWh [26]. The annual electricity use was calculated as:

$$\text{E} = \text{Rated Wattage (kW)} \times \text{L70 Lifetime (hours)} \tag{5}$$

Rated wattage values for each lamp were obtained from manufacturers' specifications. L70 lifetime is ~8000 h for 254 nm LP Hg lamps [27], ~9000 to 11,000 h for both 222 nm [28] and 265 nm [29] UV sources, and ~15,000 to 20,000 h for 365 nm [30,31] UVA LEDs. To ensure a consistent basis for comparison, each lamp was assumed to operate continuously for one full year (8760 h).

In addition to cost, the environmental impact was assessed in terms of annual equivalent carbon dioxide (eCO$_2$) emissions. This was

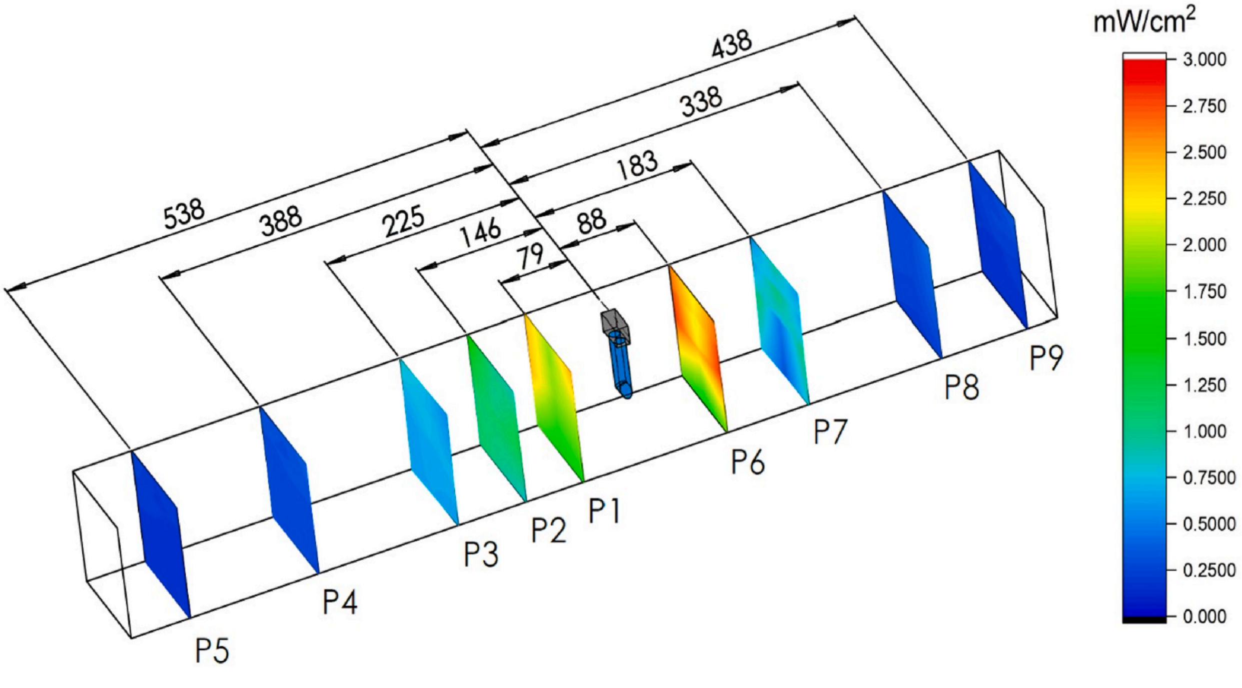

Fig. 3. Irradiance distribution of 254 nm lamp for measured planes.

computed using:

$$\text{Annual } eCO_2 = E \times Ic \tag{6}$$

where Ic is the emission factor, reported to be 0.47 kg CO_2/kWh [32]. This allows quantification of the greenhouse gas emissions associated with each lamp's electricity consumption.

To enhance the reliability and fail-safety of the system design, the measured UV dose delivered by each setup was conservatively reduced by 30 % to simulate performance at L70 conditions. This ensures that the system remains effective even when the lamp output has degraded. The required dose for a 3-log reduction (99.9 % efficiency) of *E. coli*, *MS2*, and *Phi6* was estimated using average UV rate constants reported in the literatures [11,12,14,18,25,33–35], specifically for air disinfection applications (Table S10). Once both the L70 delivered dose and the required dose were known, the initial cost and annual kWh were calculated accordingly. By integrating technical performance, economic viability, and environmental impact into a unified framework, this LCA facilitates informed decision-making for the sustainable implementation of UVGI technologies in indoor air quality management for building HVAC systems. However, it should be noted that the present analysis was limited to the operational phase (energy consumption and cost) to ensure consistent comparison across lamp types. Upstream processes (manufacturing and transport) and downstream considerations (end-of-life disposal) were not included, owing to the limited availability of reliable life cycle inventory data for emerging UV technologies.

3. Results & discussion

3.1. Irradiance characterisation of cylindrical lamps

The corrected irradiance distributions are discussed in the following sections.

3.1.1. 254 nm lamp

The spatial irradiance map for the 254 nm LP Hg lamp generated through linear interpolation is illustrated in Fig. 3. The experimental validation of the interpolation method showed deviations within ±10 %, confirming the reliability of this approach for reconstructing irradiance fields across the duct cross-section. Notably, the irradiance distribution exhibits an expected peak in proximity to the lamp surface (P1 and P6), with a gradual decay along both upstream and downstream directions. However, an intriguing observation emerges when comparing P6 and P1. Despite P1 being positioned just 79 mm downstream from the lamp surface, the plane P6, which is 9 mm farther upstream, displays slightly higher irradiance. This discrepancy is likely a result of asymmetric reflective contributions from the duct surfaces. The presence of reflective aluminum sealing tape, instrumentation mounts, and surface-mounted sensors near P6 may have intensified local irradiance through secondary reflections. Furthermore, upstream plane P7 shows an unexpected dip in irradiance, especially at the central region. This anomaly is attributed to partial obstruction by upstream sampling tubes positioned directly in front of P7, which likely cast shadows and attenuated the received UV radiation at the center of the plane. While such obstructions are physical artifacts rather than optical limitations, they highlight the importance of considering installation interference when designing in-duct UVGI systems.

At the edges of several planes (notably P1, P6, P3 and P8), elevated irradiance values appear near corners, primarily from extrapolation beyond the 3 × 3 measurement grid. These values should be interpreted with caution. Given the finite dimensions of the sensor's detection area and its limited angular response, corner interpolations are less reliable due to sparse spatial resolution and unmeasured edge reflectance. Thus, these values are likely overestimated and may not reflect the actual irradiance experienced by airborne pathogens. Overall, the irradiance pattern demonstrates a non-uniform spatial distribution closer to the lamp, strongly influenced by both lamp geometry and duct-side reflections. The relatively high irradiance near P6 and P2, along with the decline observed toward P4 and P9, suggests that peak UV disinfection zones are confined within ~20 cm of the lamp. Accurate mapping of this field is critical for validating dose delivery in UVGI systems, especially under turbulent HVAC airflow, where particle trajectories may vary significantly.

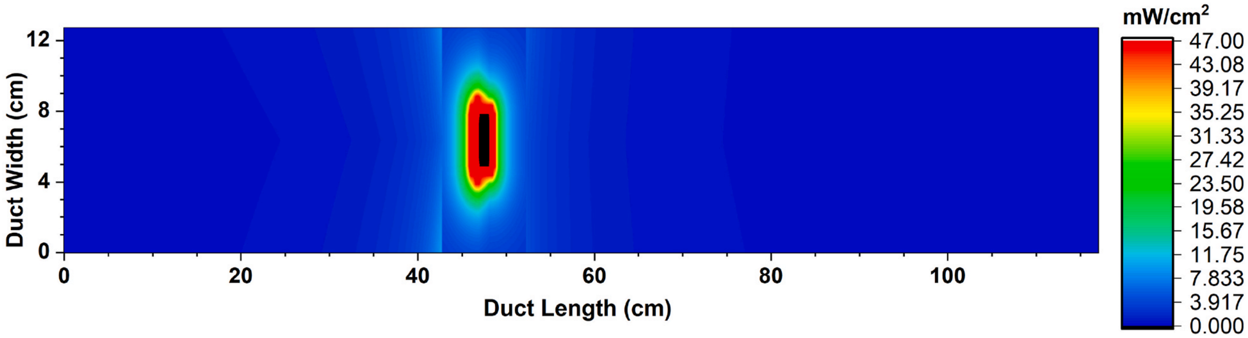

Fig. 4. Irradiance field for 254 nm lamp at the middle plane of duct (top view).

The spatial irradiance field of the 254 nm LP Hg lamp was further analyzed along the horizontal midplane of the duct to evaluate the distribution across the entire irradiated region. As illustrated in Fig. 4, irradiance reached its peak value of 47 mW/cm^2 near the lamp's surface, specifically at the lamp midpoint. To extrapolate irradiance values between measured planes, a power-law regression model was employed along the duct's length (x-direction), using the experimentally acquired data. For lateral interpolation across the duct width (y-direction), a linear approach was applied between central and peripheral planes. This hybrid interpolation technique was particularly critical near the lamp, where direct measurement was limited by physical constraints such as sensor size and lamp geometry. The application of power-law regression allowed estimation of irradiance within a 4.1 cm radius from the lamp surface (more than 3 times the lamp diameter), capturing the high-gradient zones, where irradiance transitions rapidly.

All regression-predicted irradiance values were capped at the measured maximum of 47 mW/cm^2. This conservative approach ensures that no unrealistic irradiance overshoots are introduced into the field distribution. The resulting irradiance map (Fig. 4) reveals a highly localized disinfection zone surrounding the lamp. The black region denotes the physical geometry of the lamp, while the surrounding red contour represents the irradiance peak zone. The sharp attenuation of irradiance outward from the lamp surface confirms the inverse relationship between intensity and distance from lamp, though not strictly following the inverse-square law due to significant wall reflections. This reflection-driven distortion is evident in the asymmetrical spread of irradiance contours, particularly between the 43 cm and 52 cm regions of the duct length, where interpolation shifts from regression-driven to measurement-based inputs. Although some asymmetry is visually noticeable, likely due to slight differences in measurement plane data and boundary interference, its impact is minimal from an engineering perspective. The distribution can be considered sufficiently symmetric to support its use in performance modeling, UV dose calculations, and further CFD-based airflow-disinfection interaction studies. Importantly, this irradiance field highlights that most of the effective disinfection occurs in a confined zone immediately adjacent to the UV source. This underscores the importance of strategic lamp placement and the necessity of accurate irradiance mapping to avoid overestimating system performance.

To further investigate the irradiance behavior of the 254 nm mercury lamp, the average irradiance values measured at each plane were plotted against the corresponding distance from the lamp surface (Fig. S8). Contrary to the classical inverse-square decay expected in open environments, the resulting decay profile within the duct instead exhibits a trend more closely approximating an inverse-linear relationship. This deviation is attributed to the significant internal reflections from the duct walls, which redistribute UV radiation and moderate its decay throughout the enclosure. Such reflective enhancement is absent in free-space conditions where irradiance diminishes strictly with geometric spreading, underscoring the importance of context-specific irradiance modeling in enclosed HVAC systems. The average relative error between the trend obtained from downstream measurements and the verification points was ±8 %, indicating good modelling accuracy.

For evaluating the accuracy of the proposed irradiance correction methodology, average downstream irradiance data from this study were compared against computational predictions from Luo and Zhong (2022) [25]. Their CFD-based model simulated the same in-duct UVGI setup, but without accounting for physical obstructions such as sampling tubes and sensor mounts, which are known to disrupt radiation flow in practical installations. To ensure comparability, the downstream region is a reasonable consideration for cross-verification, as it is minimally affected by those upstream obstructions. As summarized in Table 1, the benchmarked results at four axial positions demonstrate strong agreement between the corrected experimental values and the simulation outputs. Relative errors between the two datasets ranged from −18.25 % to +11.11 %, which is well within acceptable bounds for empirical validation of radiometric models, further establishing the accuracy of our measurement framework.

Notably, the higher discrepancy occurred at position closer to the lamp, where steep gradients and minor geometric misalignments can significantly influence local irradiance. At a distance of 14.7 cm from the lamp center, the measured irradiance was 0.9951 mW/cm^2, closely matching the simulated value of 1.1194 mW/cm^2, yielding a relative error of +11.1 %. Strong agreement was also observed at intermediate distances, with minimal relative errors of −4.3 % at 25.3 cm and +5.6 % at 36 cm. Although a slightly higher deviation (−18.3 %) was noted at 43.3 cm, this can be attributed to the low irradiance magnitudes and greater influence of measurement noise at farther distances from the lamp. This strong correspondence affirms that the correction factor introduced in this study, designed to account for the angular detection limitations of planar radiometric sensors, effectively improves the fidelity of in-situ irradiance characterization in reflective, in-duct environments. By bridging the gap between practical measurement limitations and computational estimations, the proposed method offers a robust framework for validating UVGI systems under real-world conditions. It also enables accurate UV dose calculations, optimized lamp placement, and the design of energy-efficient air disinfection systems.

3.1.2. 222 nm lamp

As observed from Fig. 5, the irradiance profile for measured planes demonstrates smoother transitions and enhanced uniformity

Table 1
Comparison of corrected (this study) and CFD-predicted irradiance values.

Distance from Lamp Center (cm)	Obtained Irradiance (mW/cm^2)		Relative Error (%)
	Luo and Zhong (2022) [25]	This Study	
14.7	1.119429	0.9951	11.10643
25.3	0.474333	0.4949	−4.33591
36	0.341889	0.3229	5.554111
43.3	0.211667	0.2503	−18.252

compared to the 254 nm lamp. Minor discrepancies, such as slightly elevated values at plane corners and localized dips in plane P7, were again present as discussed previously. However, the overall irradiance field was more symmetric and evenly distributed, primarily due to the dual-lamp configuration in a parallel layout, which ensured more balanced illumination across the duct's cross-section. This observation aligns with CFD simulations reported by Luo and Zhong (2022) [25].

The results of the lengthwise power-law regression applied along the duct length and linear interpolation across the width to reconstruct the full irradiance field between measured planes are presented in Fig. 6, where a broad symmetrical region of moderate irradiance is visible. The maximum measured surface irradiance was 1.75 mW/cm^2, and due to symmetry, the center region between the two lamps is expected to reach nearly double this value and is capped at this threshold to maintain physical plausibility. Like the 254 nm trend, the 222 nm data followed an inverse-linear decay (Fig. S9), although with a shallower slope. The power-law fits applied to upstream and downstream regions exhibited high fidelity with measured data, with a mean error of ±8 %.

Despite the higher total lamp power for 222 nm lamps (16 W each, adjusted based on the installation), compared to just 5 W for the 254 nm mercury lamp, the surface irradiance output was significantly lower. Specifically, the 254 nm LP Hg lamp produced irradiance over 25 times greater than the 222 nm lamp at comparable positions. This striking disparity highlights the inherently lower output efficiency of excimer technology, despite its advantages in terms of safety for human exposure. The results point to a critical area for improvement in lamp engineering and photon yield optimization. Taken together, the findings indicate that while the 222 nm excimer lamp offers more even illumination and rapid activation, its lower radiometric efficiency necessitates denser installation or longer exposure times to achieve comparable germicidal performance to mercury-based systems. However, the improved uniformity and minimal sensitivity to airflow and ambient conditions (as discussed later in Section 3.4) make it a viable candidate for occupied-space disinfection, where safety and reliability are paramount.

3.2. *Irradiance characterization of UV LEDs*

3.2.1. *265 nm LEDs*

The irradiance field of the LED modules is shown in Fig. 7. The maximum irradiance (23.5 mW/cm^2) occurred at the surfaces of the LED modules, as expected due to the strong, forward-directed beam of the diodes. The emission pattern was highly non-uniform in the central horizontal plane, with intense peaks at the module locations and pronounced drops between them. However, the top and bottom planes exhibited a more symmetric and smoothed-out distribution, confirming uniformity at the duct's vertical boundaries. Notably, the lowest irradiance occurred directly above the installed module, a consequence of the limited emission angle inherent to LED architecture. These "shadow zones," if unaddressed, could act as disinfection dead zones. Fortunately, the opposite-facing layout in this study ensured cross-coverage, mitigating the formation of dark spots and maintaining overall irradiance integrity.

The observed pattern suggests that 265 nm LED modules behave more like point sources than line sources, given their compact geometry (~5 cm in length with only four bulbs per module). The modelled average irradiance predicted trend was compared against measured verification points when all modules were active. As depicted in Fig. 8, a wave-like distribution emerged, with a sharp irradiance peak at module centers and valleys between adjacent LEDs. The comparison yielded a relative error within range of +9 % to −24 %, with average relative error of ±13 %. Affirming the reliability and predictive power of the proposed modeling approach.

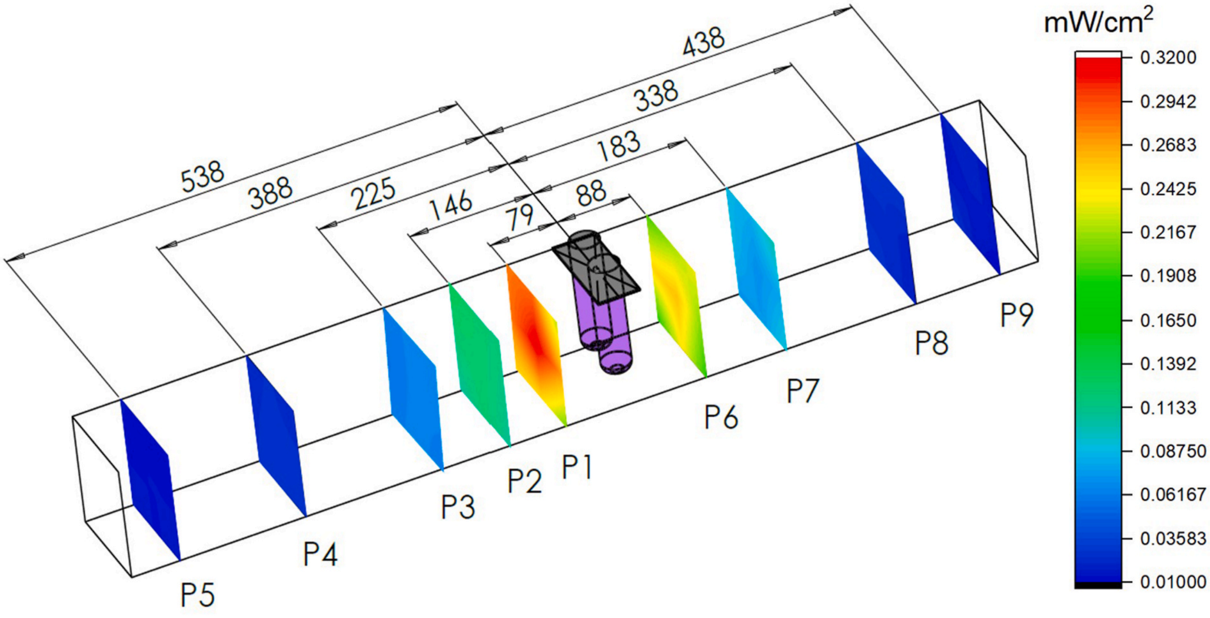

Fig. 5. Irradiance distribution of 222 nm lamp for measured planes.

]

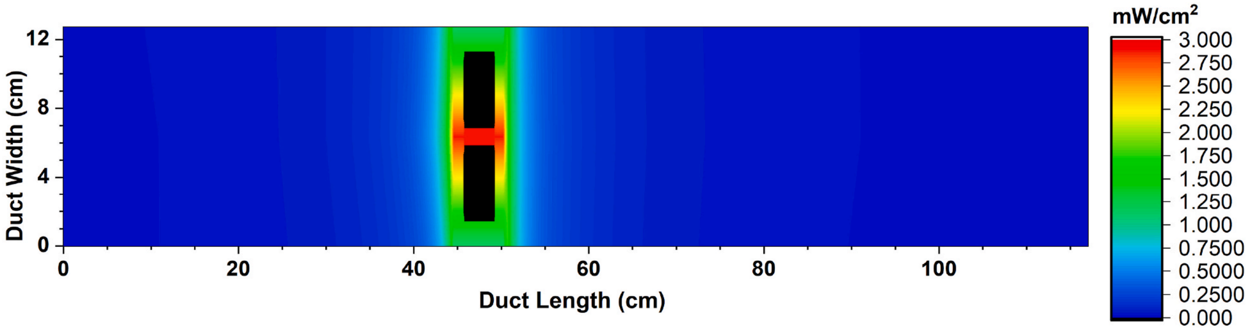

Fig. 6. Irradiance field for 222 nm lamp at the middle plane of duct (top view).

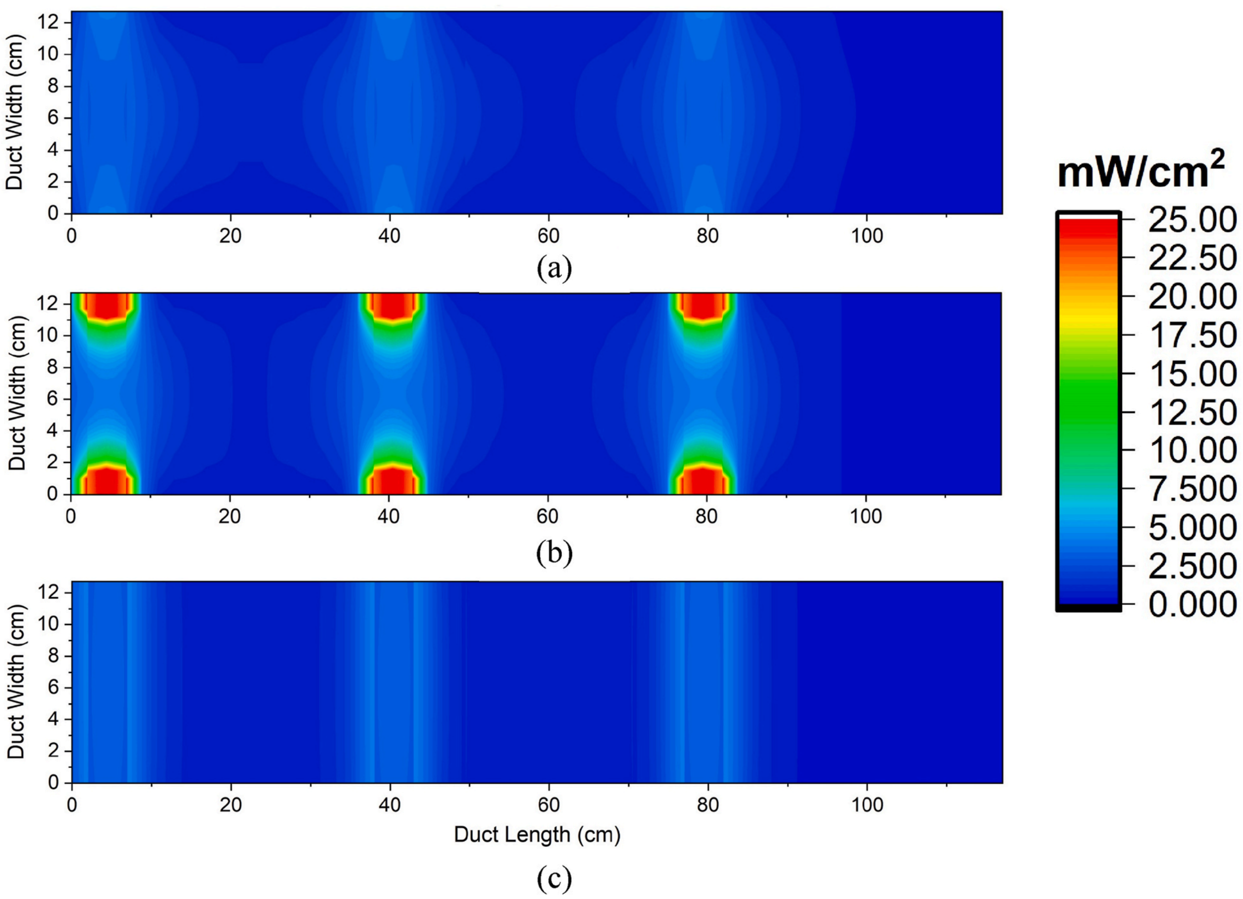

Fig. 7. 265 nm irradiance field distribution from the top view: (a) Top layer, (b) Middle Layer and (c) Bottom layer.

3.2.2. 365 nm LEDs

The irradiance field of the 365 nm LED system reveals a highly uniform distribution across the top, middle, and bottom duct planes (Fig. 9). The middle plane mirrored the installation layout of four modules on one wall and three on the other wall, creating a slightly staggered yet consistent illumination pattern. Fig. 10 illustrates the results of the modelled average irradiance distribution along the duct length, compared against experimentally measured values at randomly selected verification points. This is important for validating the predicted irradiance profile of the 365 nm LED modules under full operating conditions. The predicted irradiance curve reveals an almost constant profile, with minor fluctuations between 3.8 and 4.5 mW/cm^2, indicating a high degree of spatial uniformity across the central duct region. This uniformity is a direct consequence of the continuous zigzag arrangement of the LED modules on opposite duct walls, which ensures overlapping coverage and minimizes unexposed regions.

In contrast to the 265 nm LED system, where discrete module spacing caused pronounced irradiance troughs between modules, the

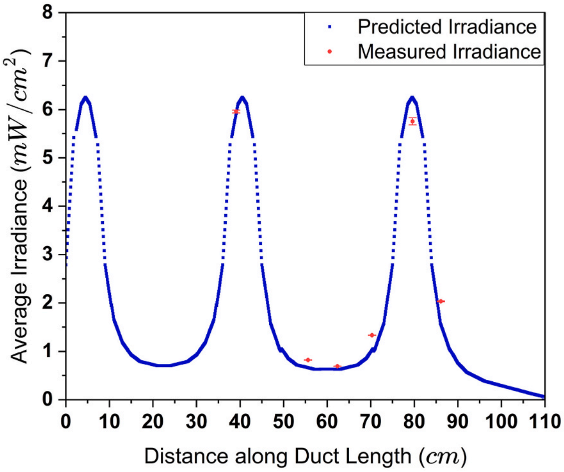

Fig. 8. 265 nm irradiance distribution along the duct length (blue region in Fig. 1).

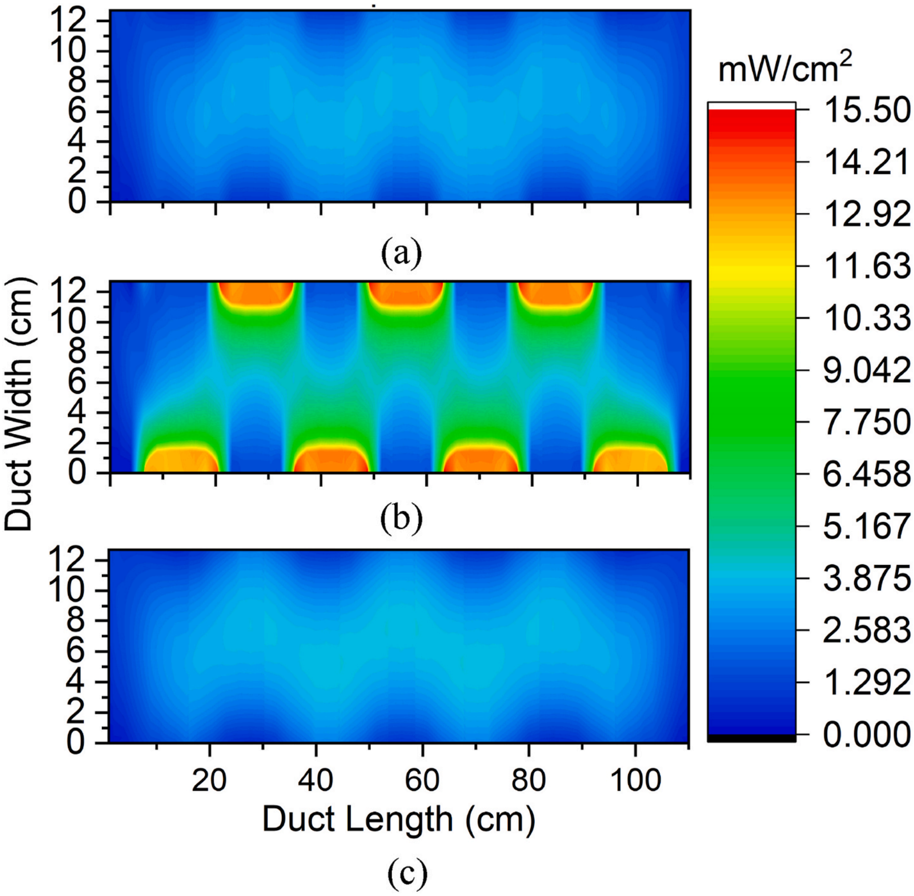

Fig. 9. 365 nm irradiance field distribution from the top view: (a) Top layer, (b) Middle Layer and (c) Bottom layer.

365 nm setup maintains consistent illumination, even at module boundaries. Despite the enhanced uniformity, the lowest irradiance levels were still consistently observed near the top and bottom edges of the duct, directly above or below the installed LED strips. These zones fall outside the primary beam angle of the LED strips and thus receive reduced irradiance. However, the coverage remains sufficient due to the strategic arrangement of multiple strips. Nevertheless, the 365 nm modules behaved more like a line source, consistent with their extended physical dimensions (each measuring 14.2 cm in length). This characteristic contrasts with the point-

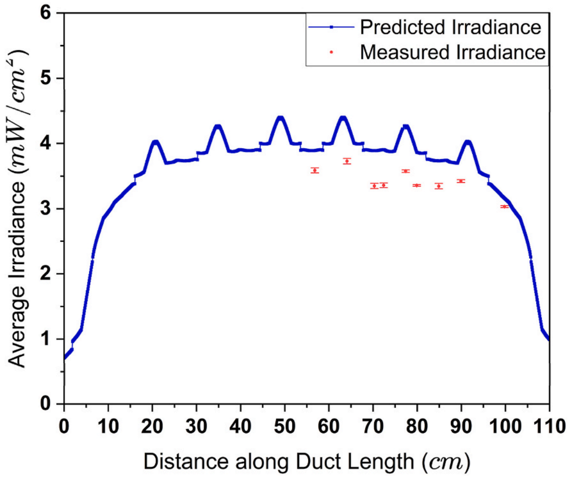

Fig. 10. 365 nm irradiance distribution along the duct length (blue region in Fig. 1).

source-like emission of the compact 265 nm modules, validating the assumption that longer LED strips (such as 365 nm LEDs) can be effectively modelled as line sources in duct-scale simulations and dose estimations. The modeling approach accounted for these characteristics and was validated against verification points, again yielding a relative error within +4 % to +19 %, with average error of ±13 %, demonstrating good agreement. This level of accuracy confirms the reliability and applicability of the modelling framework adopted in this study, particularly for systems where module spacing is minimal and emission overlap is significant.

Overall, these results highlight the practical viability of 365 nm LED arrays in applications where uniform irradiance is prioritized over germicidal efficacy. Their configuration provides excellent illumination homogeneity, making them suitable for scenarios requiring consistent UV exposure over large duct areas. However, their longer wavelength and lower germicidal effectiveness limit their standalone use for pathogen inactivation in HVAC systems compared to 265 nm or 254 nm sources. Nonetheless, their superior irradiance uniformity positions them as promising components in supplementary or multipurpose lighting-disinfection systems within HVAC applications.

3.3. Effect of correction factor

As illustrated in Fig. 11a, the average irradiance values derived using the correction factor were significantly different from those calculated without correction for distances up to 21.9 cm from the 254 nm lamp surface. Similarly, the difference between irradiance measured from a single side and the corrected multi-sided measurements was also statistically significant within the same spatial range. This underscores the critical role of angular correction in the near-field region, where sensor alignment, reflection angles, and

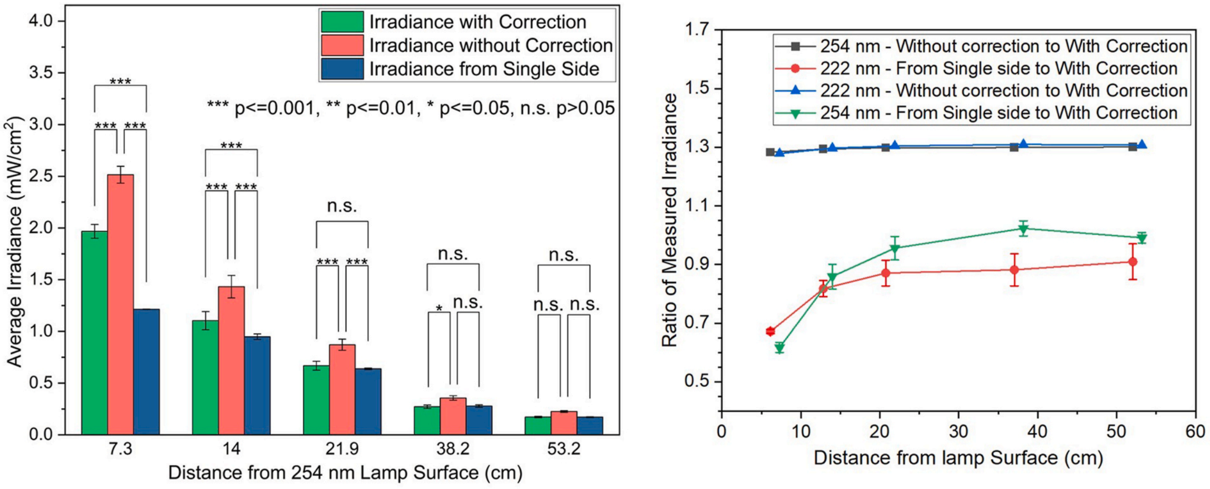

(a) (b)

Fig. 11. (a) Significance of applying the proposed correction factor; (b) Comparison of resulting irradiance values obtained using different methods.

irradiance gradients are most sensitive. Beyond 21.9 cm, the discrepancies among all three methods became statistically negligible, suggesting that single-sided measurements may be acceptable at larger distances from the lamp, where spatial irradiance becomes more diffuse and symmetric. These observations confirm that measurement precision is most critical in the high-flux zones closest to the UV source, which also corresponds to regions of highest microbial inactivation potential.

To further quantify the implications, Fig. 11b presents a line graph showing the ratio of irradiance without correction to corrected values, and the ratio of single-sided measurements to corrected values, for both 222 nm and 254 nm lamps. For planes located close to the lamp (e.g., P1), measuring irradiance from only one side underestimated irradiance by over 30 %, while multi-side measurements without correction overestimated irradiance by a similar margin. These results emphasize the dual risk of under- or overestimation when proper corrections are not applied, both of which can compromise UVGI design accuracy.

The transition distance at which single-side irradiance measurements become sufficiently accurate (defined here as within a ±10 % error margin) varies by lamp type, largely due to differences in lamp geometry. For the 254 nm LP Hg lamp, this transition occurs at approximately 17 cm from lamp surface, equivalent to roughly twice its maximum physical dimension (8.3 cm). Conversely, for the 222 nm lamp, the transition distance extends to about 37 cm, or more than three times its maximum dimension (10.5 cm). These differences arise mainly due to the multiple installed 222 nm lamps apart from the physical size and shape, which influence the angular distribution of emitted radiation. At these respective distances, each lamp begins to behave as a point source relative to the sensor's field of view. Furthermore, farther planes showed diminished sensitivity to correction due to reduced sidewall reflections, as the irradiance decays and reflections become optically insignificant. In contrast, near-field planes exhibited the highest dependency on the measurement approach due to strong angular variation, dense irradiance gradients, and reflective amplification.

The implications for LED-based systems are equally important. Unlike single-source LP Hg or excimer lamps, most LED

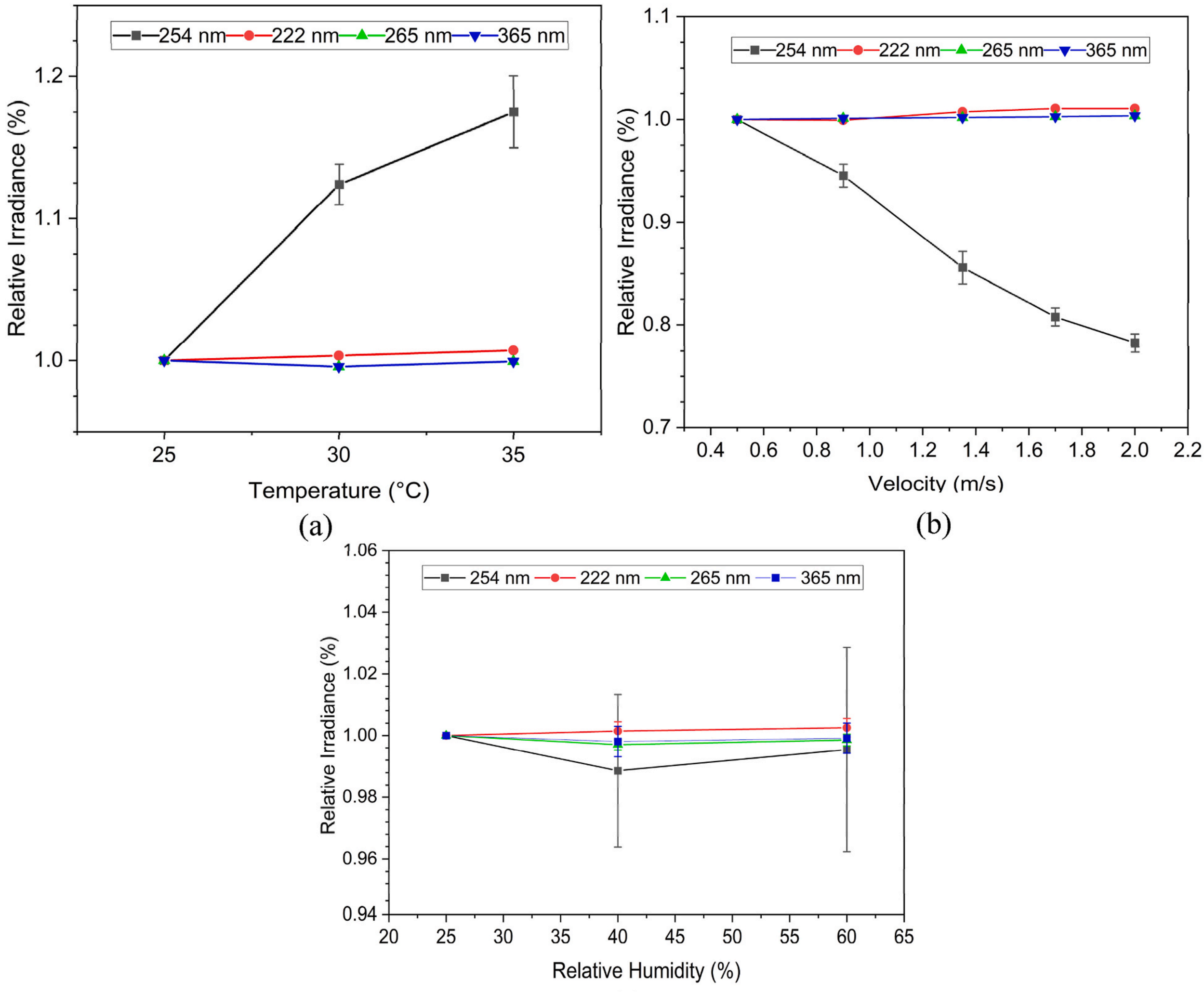

(a)

(b)

(c)

Fig. 12. Lamp output with varying air parameters: (a) Effect of temperature; (b) Effect of velocity; and (c) Effect of relative humidity (RH).

configurations involve multiple distributed modules, often installed in opposing or zigzag arrangements. These layouts inherently produce complex, directionally dependent irradiance patterns, further amplified by reflections and duct geometry. In such cases, neglecting to apply correction factors can lead to substantial cumulative errors in estimating total UV dose distribution. It is worth noting that while the correction factor presented in this study was developed based on the angular response of the ILT960 spectrometer (±60°), the approach can be extended to other radiometric sensors with known cosine response profiles, allowing broader applicability of this method in UVGI irradiance characterization.

Collectively, the findings strongly support the integration of the proposed correction factor into UVGI system characterization protocols. It enables more accurate irradiance mapping, minimizes misrepresentation in critical high-dose zones, and provides a robust foundation for dose-based design and validation of UV disinfection systems in HVAC environments.

3.4. Effect of air parameters on lamp output

The influence of key air parameters on UV lamp output is summarized in Fig. 12 for all the lamp types tested in this study. The 254 nm LP Hg lamps exhibited the most pronounced sensitivity to environmental conditions. As shown in Fig. 12a, increasing the ambient temperature from 25 °C to 35 °C resulted in a significant 18 % increase in lamp output, although the rate of increase plateaued beyond 30 °C. This behaviour reflects the thermally governed cold-spot phenomenon intrinsic to mercury lamps, where maximum UV output is typically achieved around 40 °C at the cold spot [13]. Deviations from this optimal cold-spot temperature led to reduced mercury vapor pressure and, consequently, lower UV generation. In contrast, air velocity exerted an inverse effect (Fig. 12b). As velocity increased from 0.5 m/s to 2.0 m/s, the relative irradiance decreased to approximately 80 % of baseline. This reduction is attributed to the wind-chill effect, which cools the lamp surface and lowers the mercury vapor pressure below the optimal operating range, thus diminishing the output. These findings highlight the critical importance of thermal equilibrium for mercury lamp efficacy, particularly in HVAC applications where airflow is intrinsic to operation.

However, RH levels showed no measurable impact on the lamp output within the 25–60 % range (Fig. 12c). Although, prior studies suggest that extended operation under higher RH (>60 %) can lead to condensation and surface water film formation, thereby attenuating irradiance, no such effect was observed during the typical 30 min operational period used in this study. The 222 nm far-UVC excimer lamp demonstrated remarkable thermal and aerodynamic stability, with output remaining constant across all tested temperatures, velocities, and humidity levels. This is attributed to its unique plasma-based emission mechanism, where excited-state dimers spontaneously release UV photons independently of surrounding air conditions. Unlike mercury vaporization, this excimer-driven process is largely insensitive to thermal or flow-related influences, relying primarily on input voltage and current for stability.

Conventional expectations suggest that UV LEDs are sensitive to junction temperature due to the thermal dependence of their quantum efficiency. Rising junction temperatures typically lead to reduced photon output, accelerated material degradation, and shortened lifespan. However, in this study, both 265 nm and 365 nm LEDs displayed no appreciable variation in output across the tested air temperature (25–35 °C), velocity (0.5–2.0 m/s), and RH (25–60 %) ranges. This anomaly is explained by two critical factors: (1) thermal management design — the 265 nm LED modules were equipped with active heat sinks, while the 365 nm strips benefited from duct airflow acting as a passive heat exchanger. These features stabilized junction temperatures within the nominal operational range, mitigating the risk of thermal performance loss, and (2) Limited Temperature Gradient — although prior literature reports 20–30 % output degradation over large junction temperature shifts (20 °C–120 °C) [19–21], such wide variations were not replicated in this experimental setup. The relatively narrow air temperature range tested likely produced only minor internal temperature changes, which were insufficient to significantly affect photon output. These results are further corroborated by recent findings from a leading 265 nm LED manufacturer [18], which reported negligible output variation under thermal water disinfection conditions, analogous to the cooling effect of the airflow environment in this study.

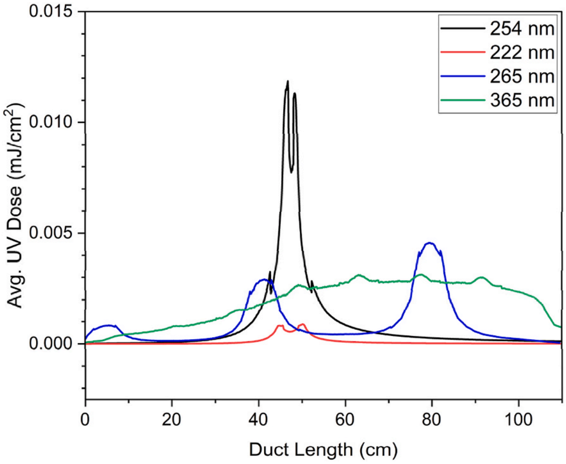

Fig. 13. UV dose distribution along the duct length (blue region in Fig. 1).

3.5. UV dose characterisation across lamp types

The dose profiles for each lamp type are presented in Fig. 13. As anticipated, the 254 nm LP Hg lamp exhibits a sharp, centralized dose peak directly in the vicinity of the lamp. This high-intensity spike results from its narrow angular emission, higher wall-plug efficiency, and collimated UV output, all of which concentrate energy deposition close to the source. The maximum UV dose for the 254 nm lamp exceeds that of the 222 nm lamp by over a factor of 13, affirming its superior radiometric power and disinfection potential.

Similarly, the 222 nm far-UVC excimer lamp shows a localized peak, albeit much lower in magnitude. This behavior underscores the inherent trade-off in using 222 nm lamps. While they offer enhanced safety for human exposure, they deliver lower energy per unit area and may require denser placement or longer exposure times for equivalent disinfection.

For the 265 nm UVC LED system, the dose distribution demonstrates a wave-like trend, directly correlating with the spatial irradiance profile previously described (see Fig. 8). Initial dose levels near the duct entrance remain low due to reduced residence time in the high turbulence mixing region, induced by the baffle. As flow stabilizes downstream, both residence time and cumulative exposure increase, yielding successively higher dose peaks in alignment with the LED module positions. In contrast, the 365 nm UVA LED system yields a relatively uniform dose distribution, with a gradual rise up to ~40 cm, followed by a plateau. This trend results from the consistent and extended irradiance field provided by the nearly continuous LED strip arrangement. While the germicidal effectiveness at this wavelength is markedly lower, the uniformity of dose delivery suggests potential for baseline photoinactivation or synergistic roles in hybrid UVGI systems.

Importantly, Fig. 13 also reveals how each lamp's dose profile reflects a balance between peak intensity and spatial coverage. The 254 nm lamp delivers intense, localized doses ideal for targeted high-risk zones, while the 365 nm lamp ensures broader area coverage with lower peak energy, which is useful for background exposure and maintenance-level disinfection. The 265 nm LEDs, with their modular flexibility, allow for customizable peak-and-valley dosing that can be tuned through spatial configuration. Irregularities and asymmetries in the LED dose profiles are indicative of complex airflow structures and residence time variation, particularly near duct inlets. These patterns highlight the need to integrate aerodynamic considerations, including velocity profiles, turbulence levels, and duct geometry, into UVGI system design. Neglecting these factors can lead to dose shadowing or overdesign, ultimately reducing energy efficiency and microbial control consistency.

Importantly, the uncertainty analysis (Table S11) revealed an overall UV dose variability of approximately ±19.1 % for the 254 nm lamp, ±22.1 % for the 222 nm lamp, ±21.7 % for the 265 nm LED, and ±19.8 % for the 365 nm LED. These values are close to those reported in UVGI literature (typically ±15 to ±20 % [25]), supporting the accuracy and reliability of the UV dose estimates obtained in this study. Furthermore, the results highlight the robustness of the framework adopted here, which combines experimental irradiance measurements with a novel angular correction factor and CFD-based exposure time estimation to provide reliable UV dose characterization across different lamp types, geometries, and installation arrangements.

In summary, these dose characterizations underscore that effective UVGI system design must account for both lamp-specific optical characteristics and duct-level fluid dynamics. Optimizing lamp position, orientation, and emission type requires balancing peak dose delivery with uniform spatial coverage to meet the desired microbial inactivation targets under real-world HVAC operating conditions.

3.6. Life-cycle analysis

Table 2 shows the values of each variable considered for the LCA, and the results are visualized in Fig. 14. As shown in Fig. 14a, the dose requirement varied by both pathogen and UV wavelength. The 222 nm excimer lamp consistently required the lowest UV doses across all organisms, demonstrating superior biological efficacy. Notably, it achieved *Phi6* inactivation with only 0.33 mJ/cm^2, nearly four times lower dose than 254 nm. The 265 nm UV-C LED outperformed the 254 nm LP Hg lamp for *E. coli* and *Phi6*, requiring 40–50 % lower doses, while both were comparable for MS2 (1.7 mJ/cm^2). Conversely, the 365 nm UVA LED required UV doses 10–25 times higher than the 254 nm lamp, confirming its limited germicidal effectiveness due to insufficient absorption of UV radiation by microbial nucleic acids at longer wavelengths.

Despite its superior microbial performance, the 222 nm excimer lamp exhibited the highest energy demands, particularly for MS2, with consumption up to 4500 kWh/year, compared to just 128 kWh/year for 254 nm (Fig. 14b). This is attributed to the low wall-plug efficiency of excimer lamps (5–15 %) and reduced microbial susceptibility of non-enveloped viruses, like MS2. The 254 nm lamp, benefitting from 30 to 38 % wall-plug efficiency [18], delivered superior energy-to-optical conversion, resulting in the lowest energy use for all three microbes. While the 265 nm UV-C LED required significantly lower doses than the 254 nm lamp, its poor electrical efficiency and thermal losses led to 6–12 times higher energy consumption.

The 365 nm UVA LED, despite its minimal germicidal activity, consumed less energy than the 222 nm lamp due to its mature technology and higher electrical efficiency (30–40 %) [18], yet it remained impractical for disinfection due to the extreme UV dose

Table 2
Average initial cost and energy (kWh) for UV lamps arrangement employed in this study.

Lamp Type	222 nm	254 nm	265 nm	365 nm
Initial cost (CAD, see Tables S6, S7, S8, and S9)	900	11	2220	240
Annual Energy Consumption (kWh, see Eq. (6))	280	44	630	149
Obtained L70 Dose (mJ/cm^2)	0.075	0.54	0.7	1.45

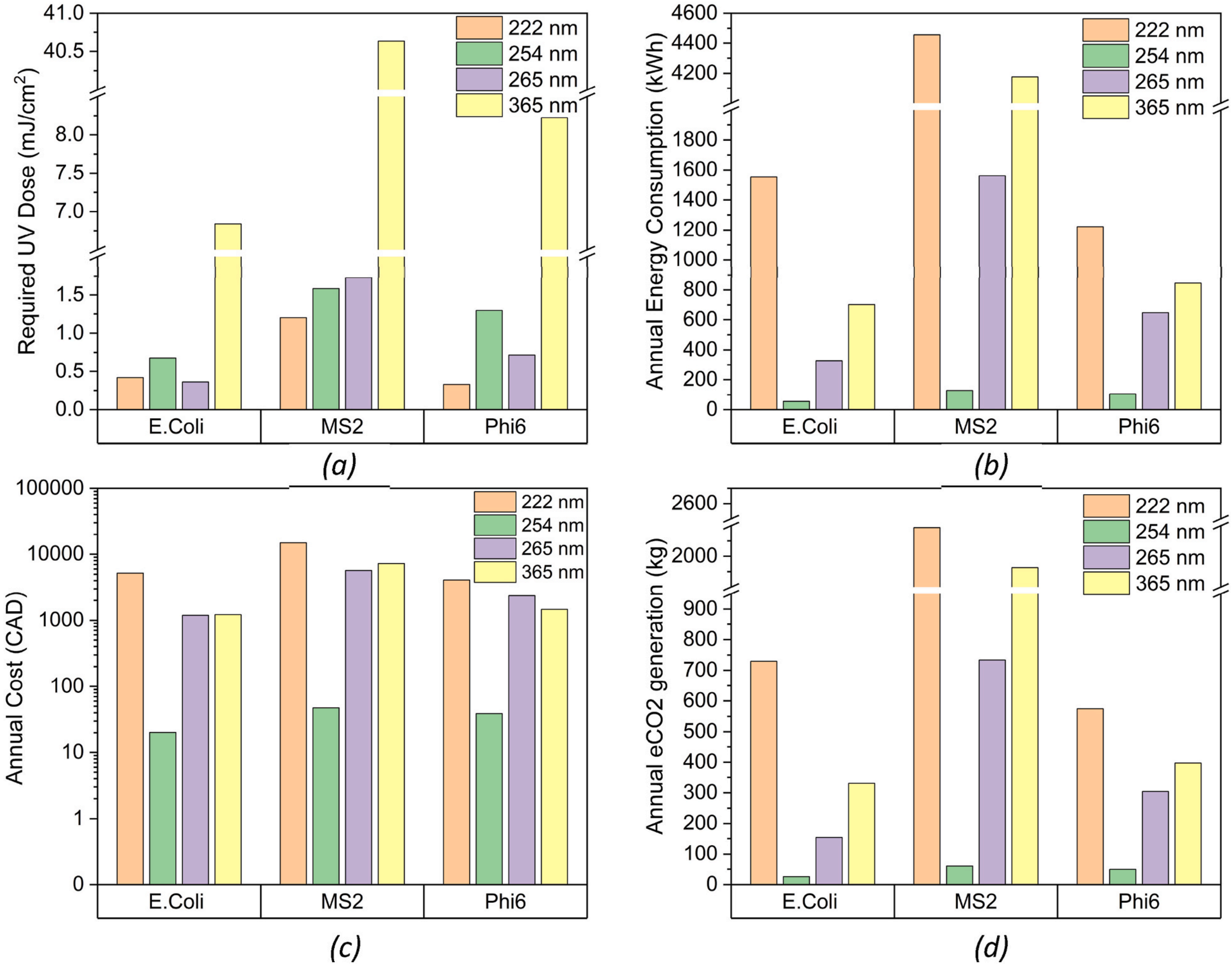

Fig. 14. LCA for UV lamps to achieve 3-log reduction of different microorganisms: (a) Required L70 UV dose (mJ/cm^2); (b) Annual energy (kWh) consumed for achieving the L70 dose; (c) Annual total cost (CAD) to achieve the target; and (d) Annual eCO$_2$ (kg) generation by the operation of lamps.

required. These trends were reflected in annual total cost (Fig. 14c) and equivalent CO$_2$ emissions (eCO$_2$) (Fig. 14d). The 254 nm LP Hg lamp remained the most economical, with annual costs under CAD 100 and emissions between 25.6 and 59.9 kg CO$_2$, depending on the pathogen. In contrast, the 222 nm lamps incurred the highest total costs, almost CAD 15000 and generated up to 2100 kg of CO$_2$ annually for MS2, making it the least sustainable option in its current form. The 265 nm LED emerged as a moderate option, with costs and emissions falling between the 222 nm and 254 nm extremes. The 365 nm LED, while relatively efficient in energy use, still showed high operating costs due to the large number of modules and power input needed to achieve effective doses.

Some technology-specific observations are worth noting. The 254 nm lamp offers the most balanced and cost-effective solution for continuous HVAC disinfection applications. However, its mercury content poses disposal and regulatory challenges, which must be accounted for in long-term sustainability planning. The 222 nm excimer lamps, despite promising biological efficacy and occupant safety, remain cost- and energy-intensive due to poor UVC output conversion efficiency. These are better suited for intermittent or localized disinfection tasks, particularly in occupied spaces. The 265 nm UVC LEDs present an emerging compromise, with better biological effectiveness and lower eCO$_2$ footprint than 222 nm, but significant room for improvement remains in thermal management, performance stability, and lifetime reliability. The 365 nm UVA LEDs, while mature in technology and efficient in power usage, are biologically inefficient for air disinfection and are unsuitable as standalone germicidal solutions in HVAC systems.

This LCA underscores the need to balance UV dose requirements with lamp efficiency in selecting UVGI systems. The results emphasize that energy efficiency, operational cost, and disinfection efficacy are tightly interlinked. The analysis also reinforces that lamp choice should be application-specific: systems requiring continuous, high-volume disinfection benefit most from 254 nm technologies, whereas intermittent or human-safe disinfection may favor 222 nm or 265 nm systems, provided further technology development enhances their UV output efficiency.

4. Conclusions

This study presents a validated, building-scale experimental framework for characterizing irradiance fields and estimating UV dose for in-duct UVGI using four source types: 222 nm excimer, 254 nm low-pressure mercury, 265 nm UVC LEDs, and 365 nm UVA LEDs. The principal methodological contribution is a novel angular correction factor for spectrometer measurements that accounts for detection-angle limitations, removing the systematic overestimation observed with uncorrected data (up to ~30 %) and reducing the maximum observed error to ~18 %. For LED systems, we introduced a scalable characterization protocol that extrapolates irradiance fields from single-module measurements to full arrays, yielding relative average errors of ±13 % and enabling flexible geometries and layouts. Propagating relative errors due to the instrument, repeatability, interpolation, and velocity terms by the root-sum-square method gives a total relative uncertainty of nearly ±20 % for UV dose, which remains within acceptable limits. Collectively, these advances constitute a transparent, technology-agnostic framework for in-duct UVGI dose characterization with stated accuracy and traceability.

Environmental testing demonstrated that air parameters influence UV output in a source-specific manner. RH had a negligible effect across all technologies. In contrast, temperature and airflow markedly affected the 254 nm LP Hg lamp, with approximately 18 % output increase with temperature rise and almost 20 % reduction at higher air velocities. With appropriate active cooling, both UVC and UVA LEDs maintained thermally stable performance within 25–35 °C, and the 222 nm excimer lamp likewise exhibited stable output under the tested air conditions. These results clarify the operating envelopes of common UV sources and the role of duct aerodynamics in governing delivered dose.

The operational LCA indicated that, under continuous in-duct duty, 254 nm LP Hg lamps provided the most favorable combination of energy use, cost, and environmental impact among the options considered. Although far-UVC excimer offers safe human exposure at 222 nm and UV LED systems offer modular flexibility and compact design, they require significantly higher operational energy and cost to achieve equivalent disinfection performance. By integrating performance testing with operational LCA on a consistent, dose-based basis, the framework enables evidence-based technology selection across a diverse range of microbial targets.

The results of this study provide essential evidence for the practical design and implementation of in-duct UVGI systems in buildings. The validated correction factor improves the accuracy of UV irradiance measurements, enabling more accurate and reliable UV dose estimation in real HVAC geometries. Quantified effects of air temperature, velocity, and relative humidity on lamp output clarify how operating conditions influence delivered dose, allowing engineers to incorporate these variations and avoid undersizing or oversizing the design. The dose-based comparison of various UV lamp types, together with metrics for energy use, total cost, and operational sustainability, provides a direct framework for selecting the most appropriate UV technology for a given air disinfection application and constraint set. Collectively, these findings support the deployment of robust, energy-efficient, cost-effective, and sustainable UVGI systems in real-life HVAC ducts to enable future pandemic-resilient buildings.

5. Recommendations

Drawing from the practical challenges encountered in this study, the following improvements are proposed to enhance future implementations.

(1) Further refinement and validation of the correction factor and irradiance are necessary, particularly in complex duct geometries and near-lamp regions where sensor access is limited. Future work should also investigate the influence of duct wall material and surface characteristics on irradiance distribution. Reflective surfaces may enhance UV irradiance by promoting secondary reflections, while absorptive or coated surfaces may reduce overall dose delivery. Incorporating such material effects into irradiance mapping and modelling would improve the applicability of UVGI system design to diverse HVAC installations.

(2) Moreover, standardizing microbial UV dose-response data across lamp types remains a key need. Expanded experimental datasets should encompass a broader spectrum of airborne microorganisms, including enveloped and non-enveloped viruses, spores, and fungal aerosols, to strengthen dose modeling and disinfection predictions.

(3) To enhance the practicability of LCA, future studies should integrate a broader range of microbial surrogates and real-world design variables, including lamp quantity, geometry, duct mounting configurations, and airflow patterns. Scaling considerations and market-specific wattage options must be factored in to assess economic and energy implications realistically. Importantly, pre- and post-operational phases, including raw material extraction, manufacturing, and end-of-life disposal, especially for mercury-based systems, should be incorporated to enable cradle-to-grave environmental impact assessments.

(4) More so, incorporating seasonal and climatic variability, such as changes in ventilation rates, air temperature, and RH, would improve system-level integration of UVGI technologies within the building energy framework. Additionally, regional variations in electricity grid carbon intensity must be accounted for, as the environmental footprint of energy-intensive systems can vary significantly between fossil-fuel and renewable-dominated regions.

(5) Finally, future work should rigorously investigate lamp degradation behaviors under different operational modes. Studies examining on–off cycling effects, thermal fatigue, intensity depreciation, and lamp burnout will be vital for defining performance reliability and failure thresholds, especially for LED systems where lifetime claims remain uncertain. Such data will support optimized deployment strategies for continuous versus occupancy-based disinfection, ensuring long-term viability and effectiveness of UVGI interventions in diverse environments. It should be noted that this study was constrained by the specifications of commercially available lamp models at the time of testing. With rapid advances in UVC and UVA LED technology, including improvements in wall-plug efficiency and thermal stability, the performance benchmarks reported here are expected

to improve in future systems. Nevertheless, the experimental framework and LCA methodology developed in this study remain directly applicable to next-generation sources.

CRediT authorship contribution statement

Jay Patel: Writing – original draft, Visualization, Validation, Methodology, Investigation, Formal analysis, Data curation, Conceptualization. **Sunday S. Nunayon:** Writing – review & editing, Project administration. **Lexuan Zhong:** Writing – review & editing, Supervision, Resources, Project administration, Funding acquisition.

Declaration of competing interest

The authors declare that they have no known competing financial interests or personal relationships that could have appeared to influence the work reported in this paper.

Acknowledgments

This research was supported by the Natural Sciences and Engineering Research Council of Canada (NSERC) through the Alliance Program (ALLRP 560993–20). We also gratefully acknowledge Engineered Air for their financial support and technical contributions to this study.

Appendix A. Supplementary data

Supplementary data to this article can be found online at https://doi.org/10.1016/j.jobe.2025.114244.

Data availability

Data will be made available on request.

References

[1] Method of Testing General Ventilation Air-Cleaning Devices for Removal Efficiency by Particle Size, 2017. (Accessed 29 May 2025).

[2] B. Stephens, J.A. Siegel, Comparison of test methods for determining the particle removal efficiency of filters in residential and light-commercial central HVAC systems, Aerosol. Sci. Technol. 46 (2012) 504–513, https://doi.org/10.1080/02786826.2011.642825.

[3] Z. Lu, W.Z. Lu, J.L. Zhang, D.X. Sun, Microorganisms and particles in AHU systems: measurement and analysis, Build. Environ. 44 (2009) 694–698, https://doi.org/10.1016/J.BUILDENV.2008.05.014.

[4] Z. Liu, C. Lin, J. Shi, M. Ding, H. Liu, J. Chu, H. Li, Z. Huang, X. Xiao, T. Wan, J. He, Evaluation of upper-room ultraviolet germicidal irradiation system for air disinfection and energy conservation in multi-patient ward, J. Build. Eng. 93 (2024) 109885, https://doi.org/10.1016/J.JOBE.2024.109885.

[5] Z. Liu, S. Ma, G. Cao, C. Meng, B.J. He, Distribution characteristics, growth, reproduction and transmission modes and control strategies for microbial contamination in HVAC systems: a literature review, Energy Build. 177 (2018) 77–95, https://doi.org/10.1016/J.ENBUILD.2018.07.050.

[6] R. Huang, I. Agranovski, O. Pyankov, S. Grinshpun, Removal of viable bioaerosol particles with a low-efficiency HVAC filter enhanced by continuous emission of unipolar air ions, Indoor Air 18 (2008) 106–112, https://doi.org/10.1111/J.1600-0668.2007.00512.X.

[7] L. Abkar, K. Zimmermann, F. Dixit, A. Kheyrandish, M. Mohseni, COVID-19 pandemic lesson learned- critical parameters and research needs for UVC inactivation of viral aerosols, Journal of Hazardous Materials Advances 8 (2022) 100183, https://doi.org/10.1016/J.HAZADV.2022.100183.

[8] A. Rebecca, D.O. Woo, A. Guha, An energy efficiency and cost analysis of utilizing high-intensity profile UVC systems on air handling unit under cool-humid climate, Build. Environ. 265 (2024) 111989, https://doi.org/10.1016/J.BUILDENV.2024.111989.

[9] J.A. Guerrero-Beltrán, G.V. Barbosa-Cánovas, Advantages and Limitations on Processing Foods by UV Light, 2004, pp. 137–147, https://doi.org/10.1177/1082013204044359, 10.1177/1082013204044359 10.

[10] C.M.A.P. Franz, I. Specht, G.S. Cho, V. Graef, M.R. Stahl, UV-C-inactivation of microorganisms in naturally cloudy apple juice using novel inactivation equipment based on Dean vortex technology, Food Control 20 (2009) 1103–1107, https://doi.org/10.1016/J.FOODCONT.2009.02.010.

[11] H. Luo, L. Zhong, Ultraviolet germicidal irradiation (UVGI) for in-duct airborne bioaerosol disinfection: review and analysis of design factors, Build. Environ. 197 (2021) 107852, https://doi.org/10.1016/J.BUILDENV.2021.107852.

[12] H. Zhang, A.C.K. Lai, Evaluation of single-pass disinfection performance of Far-UVC light on airborne microorganisms in duct flows, Environ. Sci. Technol. 56 (2022) 17849–17857, https://doi.org/10.1021/ACS.EST.2C04861.

[13] J. Lau, W. Bahnfleth, J. Freihaut, Estimating the effects of ambient conditions on the performance of UVGI air cleaners, Build. Environ. 44 (2009) 1362–1370, https://doi.org/10.1016/J.BUILDENV.2008.05.015.

[14] Y. Yang, H. Zhang, S.S. Nunayon, V. Chan, A.C.K. Lai, Disinfection efficacy of ultraviolet germicidal irradiation on airborne bacteria in ventilation ducts, Indoor Air 28 (2018) 806–817, https://doi.org/10.1111/ina.12504.

[15] H. Zhang, X. Jin, S.S. Nunayon, A.C.K. Lai, Disinfection by in-duct ultraviolet lamps under different environmental conditions in turbulent airflows, Indoor Air 30 (2020) 500–511, https://doi.org/10.1111/INA.12642.

[16] M.H. Wang, H.H. Zhang, C.K. Chan, P.K.H. Lee, A.C.K. Lai, Experimental study of the disinfection performance of a 222-nm Far-UVC upper-room system on airborne microorganisms in a full-scale chamber, Build. Environ. 236 (2023) 110260, https://doi.org/10.1016/J.BUILDENV.2023.110260.

[17] S.S. Nunayon, H.H. Zhang, A.C.K. Lai, A novel upper-room UVC-LED irradiation system for disinfection of indoor bioaerosols under different operating and airflow conditions, J. Hazard Mater. 396 (2020) 122715, https://doi.org/10.1016/J.JHAZMAT.2020.122715.

[18] Y.H. Lu, R.X. Wang, H.L. Liu, A.C.K. Lai, Evaluating the performance of UV disinfection across the 222-365 nm spectrum against aerosolized bacteria and viruses, Environ. Sci. Technol. 58 (2024) 6868–6877, https://doi.org/10.1021/ACS.EST.3C08675/SUPPL_FILE/ES3C08675_SI_001.PDF.

[19] S.-H. Lin, M.-C. Tseng, R.-H. Horng, R.-H. Horng, S. Lai, K.-W. Peng, M.-C. Shen, D.-S. Wuu, D.-S. Wuu, S.-Y. Lien, H.-C. Kuo, H.-C. Kuo, Z. Chen, Z. Chen, T. Wu, T. Wu, Thermal behavior of AlGaN-based deep-UV LEDs, Opt. Express 30 (Issue 10) (2022) 16827–16836, https://doi.org/10.1364/OE.457740. Ppp. 16827–16836 30.

[20] K.-W. Peng, M.-C. Tseng, S.-H. Lin, S. Lai, M.-C. Shen, D.-S. Wuu, D.-S. Wuu, R.-H. Horng, R.-H. Horng, Z. Chen, Z. Chen, T. Wu, Sidewall geometric effect on the performance of AlGaN-based deep-ultraviolet light-emitting diodes, Opt. Express 30 (26) (2022) 47792–47800, https://doi.org/10.1364/OE.475219. Ppp. 47792–47800 30.

[21] Ł. Gryko, U.J. Błaszczak, M. Zajkowski, The impact of time and temperature of operation on the characteristics of high-power UVC LEDs and their disinfection efficiency, Appl. Sci. 13 (2023) 12886, https://doi.org/10.3390/APP132312886. Page 12886 13 (2023).

[22] Discover our Temperature-independent UV-C Leds | AquiSense Inc., (n.d.). https://aquisense.com/temperature-independent/(accessed May 10, 2025).

[23] Y. Wu, Y. Wang, J. Liu, X. Xu, Y. Song, X. Zhang, L. Jiang, P. Chen, Effects of distance, temperature, and relative humidity on the irradiance of Ultraviolet-C germicidal lamp: a quantitative Study, Indoor Air 2024 (2024) 1951792, https://doi.org/10.1155/2024/1951792.

[24] J. Wu, H. Luo, L. Zhong, Development of a multi-functional HVAC facility for the evaluation of air cleaning technologies and ventilation performance. https://doi.org/10.7939/R3-WGYS-F764, 2022.

[25] H. Luo, L. Zhong, Development and experimental validation of an improved mathematical irradiance model for in-duct ultraviolet germicidal irradiation (UVGI) applications, Build. Environ. 226 (2022) 109699, https://doi.org/10.1016/J.BUILDENV.2022.109699.

[26] Utilities consumer advocate: regulated rates - year at a glance, (n.d.). https://ucahelps.alberta.ca/your-utilities/rates/regulated-rates/(accessed May 31, 2025).

[27] A. Semenov, R. Kharak, Y. Bychkov, V. Dudnyk, B. Yeleussinov, Method of predicting the useful life of ultraviolet lamps in electrotechnical systems under UV radiation, Prz. Elektrotechn. (2024) 280–283, https://doi.org/10.15199/48.2024.08.56.

[28] Ushio Publishes Life Test Results of Filtered Care222® Modules | Ushio America, Inc., (n.d.). https://www.ushio.com/ushio-publishes-life-test-results-of-filtered-care222-modules/(accessed May 31, 2025).

[29] J. Ruschel, J. Glaab, N. Susilo, S. Hagedorn, S. Walde, E. Ziffer, H.K. Cho, N.L. Ploch, T. Wernicke, M. Weyers, S. Einfeldt, M. Kneissl, Reliability of UVC LEDs fabricated on AlN/sapphire templates with different threading dislocation densities, Appl. Phys. Lett. 117 (2020), https://doi.org/10.1063/5.0027769.

[30] F.J. Arques-Orobon, M. Vazquez, N. Nuñez, Lifetime Analysis of Commercial 3 W UV-A LED, Crystals 10 (2020) 1083, https://doi.org/10.3390/CRYST10121083. Page 1083 10 (2020).

[31] T. Mukai, D. Morita, M. Yamamoto, K. Akaishi, K. Matoba, K. Yasutomo, Y. Kasai, M. Sano, S.I. Nagahama, Investigation of optical-output-power degradation in 365-nm UV-LEDs, Physica Status Solidi (C) Current Topics in Solid State Physics 3 (2006) 2211–2214, https://doi.org/10.1002/PSSC.200565354.

[32] Alberta's greenhouse gas emissions reduction performance | Alberta.ca, (n.d.). https://www.alberta.ca/albertas-greenhouse-gas-emissions-reduction-performance (accessed May 31, 2025).

[33] Y.H. Lu, H. Wu, H.H. Zhang, W.S. Li, A.C.K. Lai, Synergistic disinfection of aerosolized bacteria and bacteriophage by far-UVC (222-nm) and negative air ions, J. Hazard Mater. 441 (2023) 129876, https://doi.org/10.1016/J.JHAZMAT.2022.129876.

[34] C.C. Tseng, C.S. Li, Inactivation of virus-containing aerosols by ultraviolet germicidal irradiation, Aerosol. Sci. Technol. 39 (2005) 1136–1142, https://doi.org/10.1080/02786820500428575.

[35] W.J. Snelling, A. Afkhami, H.L. Turkington, C. Carlisle, S.L. Cosby, J.W.J. Hamilton, N.G. Ternan, P.S.M. Dunlop, Efficacy of single pass UVC air treatment for the inactivation of coronavirus, MS2 coliphage and Staphylococcus aureus bioaerosols, J. Aerosol Sci. 164 (2022) 106003, https://doi.org/10.1016/J.JAEROSCI.2022.106003.